Mean shift based gradient vector flow for image segmentation

Zhou, H., Li, X., Schaefer, G., Emre Celebi, M., & Miller, P. (2013). Mean shift based gradient vector flow for image segmentation. *Computer Vision and Image Understanding*, *117*(9), 1004-1016. https://doi.org/10.1016/j.cviu.2012.11.015

Published in:
Computer Vision and Image Understanding

Document Version:
Peer reviewed version

Queen's University Belfast - Research Portal:
Link to publication record in Queen's University Belfast Research Portal

Mean Shift Based Gradient Vector Flow For Image Segmentation

Huiyu Zhou[a,*], Xuelong Li[b], Gerald Schaefer[c], M. Emre Celebi[d], Paul Miller[a]

[a] *ECIT, Queen's University Belfast, Belfast, BT3 9DT, United Kingdom*
[b] *Center for OPTical IMagery Analysis and Learning (OPTIMAL), State Key Laboratory of Transient Optics and Photonics, Xi'an Institute of Optics and Precision Mechanics, Chinese Academy of Sciences, Xi'an 710119, Shaanxi, P. R. China. E-mail: xuelong_li@opt.ac.cn.*
[c] *Department of Computer Science, Loughborough University, Loughborough, LE11 3TU, United Kingdom*
[d] *Department of Computer Science, Louisiana State University, Shreveport, LA 71115, United States*

Abstract

In recent years, gradient vector flow (GVF) based algorithms have been successfully used to segment a variety of 2-D and 3-D imagery. However, due to the compromise of internal and external energy forces within the resulting partial differential equations, these methods may lead to biased segmentation results. In this paper, we propose MSGVF, a mean shift based GVF segmentation algorithm that can successfully locate the correct borders. MSGVF is developed so that when the contour reaches equilibrium, the various forces resulting from the different energy terms are balanced. In addition, the smoothness constraint of image pixels is kept so that over- or under-segmentation can be reduced. Experimental results on publicly accessible datasets of dermoscopic and optic disc images demonstrate that the proposed method effectively detects the borders of the objects of interest.

Keywords: Image segmentation, mean shift, gradient vector flow, contour, energy function.

*Corresponding author. Tel: +44-28-90971753; fax: +44-28-90971702.
Email address: h.zhou@ecit.qub.ac.uk (Huiyu Zhou)

1. Introduction

Snakes or active contour models were first proposed by Kass *et al.* in 1987 [1]. Snakes or active contours refer to curves or surfaces that are defined within the image domain with external constraint forces, and driven by image forces towards the image features such as edges. Since their publication, these deformable models have received tremendous attention in the research community [2, 3, 4, 5].

According to the representation and implementation, there are mainly two groups of deformable models: parametric deformable models (PDMs) and geometric deformable models (GDMs) [6]. GDMs describe curves or surfaces as level sets of higher-dimensional scalar functions that evolve in an Eulerian style, while PDMs explicitly parameterise curves or surfaces in a Lagrangian fashion [6]. With remarkable success, these established models continuously target the following two major technical problems: initialisation (or capture range) [7],[8] and topological changes [9],[10]. On the other hand, there are also some interesting work related to nonparametric active contours, which may render the boundary settlement independent of the initialisation process, e.g. [11, 12].

GDMs are often used to address topological flexibility. For example, Caselles *et al.* applied curve evolution theory [13] and developed a geometric active contour model [14], while Malladi *et al.* introduced a geometric active contour model [15] based on the level set principle [16]. Han *et al.* [6] reported a topology-preserving level set method that achieved topology preservation using the simple point concept. However, GDMs still face a number of challenges in different aspects. For example, in a level set scheme (one example of GDMs), topological constraints on the evolving boundary need to be released in order for the scheme to deal with a higher dimensional space [17]. Furthermore, GDMs can be further improved in the detection of boundary gaps [18].

PDMs have been widely used in boundary detection, motion detection and tracking, and object recognition. A number of algorithms have been established for various applications by formulating new forms of the external energy in the Snake model. These algorithms include balloons [19], distance potential force [20], diffusion Snakes [21], gradient vector flow (GVF) [22] and its generalisation [23], and further developments [24, 25]. GVF and its variants have achieved tremendous success by attracting the active contour towards object boundaries from a relatively large distance. These approaches are also capable of converging to object cavities in some applications. In spite of this progress, evidence shows that the performance of

PDMs needs to be improved in automatic initialisation and splitting [10].

In recent years, numerous efforts have been made to provide potential solutions towards the capture range or/and topological change problems. A comprehensive survey has been reported in [26]. For example, a graph theory based approach was introduced by Li *et al.* [10] within the external force term in the Snake model to perform automatic Snake initialisation or splitting. Chuang and Lie [27] presented a downstream algorithm based on an extended GVF field model, where the downstream process starts with a set of selected seeds by considering local gradient direction information around each pixel. Yang *et al.* [28] proposed a robust colour GVF Snake model which combines robust estimation and colour gradients using an L_2E robust estimation. Vasilevskiy and Siddiqi [29] demonstrated that their gradient flow model can be used to maximise the rate of the flux of a vector field in a two- or three-dimensional domain. This model can drive the vector field to go along with outstanding magnitudes.

Paragios *et al.* [25] proposed an edge driven bi-direction geometric flow for boundary detection by combining the geodesic active contour flow [30] and the gradient vector flow model [22]. Tang and Acton [31] proposed a multiscale gradient vector flow to elude clutter and to reliably localize the vessel boundaries. Afterwards, Tang [32] presented a cancer image segmentation algorithm, where the first part uses an anisotropic diffusion filter for removing the noise and hairs, and the second part uses a multi-directional GVF Snake to segment the suspicious areas. A motion gradient vector flow model for tracking rolling leukocytes was introduced by Ray and Acton [33] and utilises the direction of leukocyte movement. Michailovich *et al.* [34] developed an energy functional based on the Bhattacharyya distance to drive curves towards the shape that embeds a maximal discrepancy between the empirical distributions of the photometric variable inside and outside the contours.

In this paper, we propose a new type of dynamic energy force for Snakes combining local GVFs with mean shift. Our approach is largely different from [35] that pursued a smooth vector field, where the contour evolution relied on the summation of the current gradient vector and the mean difference of all the gradients. The proposed MSGVF scheme in our work seeks an optimal solution to a newly designed Euler-Lagrangian function that simulates the energy minimisation of the evolving contour. Our algorithm is developed in the way that both local (GVF) and global (mean shift) energy minimisation are balanced, whilst the smoothness constraint of the image pixels is kept. The proposed approach also significantly differs from those published in [24, 36, 37, 38, 39]: our method uses a Lagrange multiplier to

integrate the classical GVF and the mass density function of the boundary into a combinatorial form. The boundary is considered as a solution of the introduced Partial Differential Equation (PDE), and we use mean shift as an optimisation approach to simplify the PDE computation. Comparably, the classical approaches investigated the distance between the two centroids of the previous and the present closed boundaries, where truncated Taylor series gives a good approximation to the parameters used in the classical Gradient Vector Flow. Mean shift was used as a stopping criterion for the segmentation, and theoretical analysis for the asymptotic properties was also given in the publications.

The remainder of the paper is organised as follows. In the next section, the proposed Mean Shift based Gradient Vector Flow (MSGVF) algorithm is presented. Section 3 provides experimental results and performance analysis. Finally, conclusions and future work are given in Section 4.

2. Mean Shift based GVF algorithm (MSGVF)

2.1. Traditional Snakes and GVF

Snake (or active contour) models are used to detect object boundaries or edges, given an initial guess of the evolving contours by the user. The major challenge is to search for a global minimum over a non-convex functional under predefined constraints, which leads to the desired solution [1]. Both initial and boundary conditions appear very important as they significantly affect the search for a contour of both global and local minimums. This has been justified by the evidence that the evolving boundary can vanish into a single point at a global minimum of the potential [9].

Classical Snake models consider a combination of internal and external energy, in which the boundary will stop evolving when an energy balance is obtained. The external energy force in the Snake model is restricted to a small area which is close to the real boundary. If it is far from the real boundary, the Snake may have difficulty in converging to the correct position due to image noise or distractions that violate the objective function. To address this, Xu *et al.* [22] proposed a GVF field map to represent the external energy force in the Snake model. This GVF term is sensitive to the object boundaries or edges appearing in the image and hence effectively pushes the Snakes towards the real edges.

Let a Snake be a curve $\mathbf{x}(s) = [x(s), y(s)], s \in [0, 1]$, which evolves in an image domain to reach a minimisation of the following energy function:

$$E(\mathbf{x}) = \int_0^1 \Big[\frac{1}{2}\Big(\alpha\Big|\frac{\partial \mathbf{x}}{\partial s}\Big|^2 + \beta\Big|\frac{\partial^2 \mathbf{x}}{\partial s^2}\Big|^2\Big) + E_{ext}(\mathbf{x})\Big] ds, \tag{1}$$

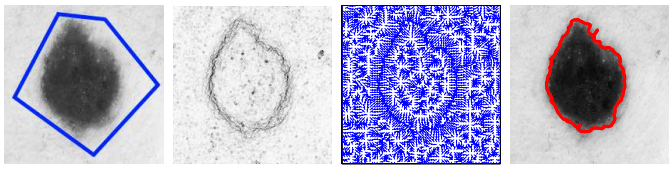

(a) (b) (c) (d)

Figure 1: Example of GVF segmentation: (a) Original image with the initial contour, (b) edge enhancement, (c) GVF field map and (d) final contour settlement (red color). The parameters used in this example are $\alpha = 0.1$, $\beta = 0.01$, $\gamma = 1$, $\kappa = 0.6$. Better viewed in colour.

where α and β are the weights that determine the tension and rigidity of the Snake respectively. The first order derivative $\frac{\partial \mathbf{x}}{\partial s}$ causes stretching while the second order derivative $\frac{\partial^2 \mathbf{x}}{\partial s^2}$ leads to bending. The first two terms on the right-hand side of Eq. (1) are referred to as the internal energy of the Snake, and the third term is the external energy that attains small values at the feature points. In the presence of high gradients at image boundaries (e.g. step edges) the external energy is represented by $-\bigtriangledown (G_\sigma(x,y) * I(x,y))^2$. In the case of line drawings, $\pm G_\sigma(x,y) * I(x,y)$ is used instead, where G_σ is a two-dimensional Gaussian function with standard deviation σ.

To obtain a minimisation, the contour should satisfy the following time-dependent function:

$$\gamma \frac{\partial \mathbf{x}}{\partial t} = \frac{\partial}{\partial s}\Big(\alpha \frac{\partial \mathbf{x}}{\partial s}\Big) - \frac{\partial^2}{\partial s^2}\Big(\beta \frac{\partial^2 \mathbf{x}}{\partial s^2}\Big) - \bigtriangledown E_{ext}(\mathbf{x}) = 0, \tag{2}$$

where γ is the coefficient. In GVF Snakes, the external energy of Eq. (2), $-\bigtriangledown E_{ext}(\mathbf{x})$, is replaced by a GVF field, which is defined as the solution of the following Euler equations using the calculus of variations [40]:

$$\begin{cases} \mathbf{v}_t = \mu \bigtriangledown^2 \mathbf{v} - (\mathbf{v} - \bigtriangledown f)|\bigtriangledown f|^2, \\ \mathbf{v}_0 = \bigtriangledown f, \end{cases} \tag{3}$$

where $\mathbf{v}_t$ is the partial derivative of $\mathbf{v}$ with respect to t, $\bigtriangledown^2 = \frac{\partial^2}{\partial x^2} + \frac{\partial^2}{\partial y^2}$, and f indicates an edge map of the image and attains large values at feature points. Fig. 1 illustrates an example of GVF segmentation, where the edges are enhanced via Gaussian filtering, and the GVF field map is calculated according to the solution of Eq. (3).

The classical GVF Snake appears to be less effective in the presence of distractions or noise in the vicinity of a real boundary (see the experimental

section). As one of the possible solutions to this problem, in the previous work, we proposed a mean shift based GVF strategy [24, 38]: when the internal and external forces of the GVF Snake are balanced, we have the Euler equation as follows:

$$g_1(d)C''(s) - g_2(d^{-1})C''''(s) + g_3(d)V = 0, \tag{4}$$

where $g_1(d)$, $g_2(d^{-1})$ and $g_3(d)$ are the *weighting functionals* of the internal and external energy terms, respectively, $C(s)$ is the contour that delineates the desired boundaries and d is the Euclidean distance between the presumed centroid of the real boundary and the estimated one of the snake.

According to [39], after appropriate variations, Eq. (4) has a deformable form as $\tilde{\alpha}dC''(s) - \frac{\tilde{\beta}}{d}C''''(s) + \gamma V = 0$, where $\tilde{\alpha} = \tilde{g}_1(d_1)$, $\tilde{\beta} = \tilde{g}_2(d_2)$, d_1 and d_2 are two constants, and $\tilde{g}_1$ and $\tilde{g}_2$ are the variations of the functionals g_1 and g_2. The Euclidean distance between the two centroids, d, is proportional to the average mean shift of the entire contour [38]. This is motivated by the fact that upon the settlement of the Snake, these two centroids must be able to match.

2.2. Contour deformation

As discussed above, the settlement of Snakes relies on the interaction between the internal and external energy forces. If one of them has a larger force than the other, the Snake will penalise the other term and hence the Snake's settlement may be biased, leading to over- or under-segmentation. In the situation where there exists strong image noise or distractions next to the target contour, a denoising process must be properly designed in order to handle the bias issue. Fig. 2 illustrates dermoscopic images (a) with their blurred outcomes (b) using a Gaussian filter in order to reduce noise during the GVF segmentation procedure. However, a new challenge is that we have no prior information about the level of image noise and the locations of distractions and hence appropriate noise reduction may be very difficult to achieve.

Another possible solution is to re-design the energy functional considering the combinatorial effects of the internal and external energy forces within the objective function, i.e. Eq. (1). As a result, the newly designed functional must be adaptive to different image circumstances. In particular, if the internal energy term dominates the evolution of the contour, the external energy term will be used to constrain the diffusion of the evolutionary contour in order to prevent over-evolution of the contour. Here, we take a close look at the evolution of the contour with numerical modelling,

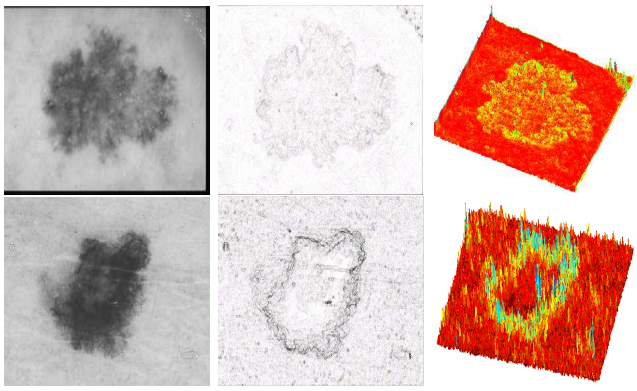

(a) (b) (c)

Figure 2: Examples of ambiguous boundary detection that can result in under- or over-segmentation (see the peaks in the graphs): (a) Original image, (b) image blurring by Gaussian filtering and (c) volumetric representation of (b). Better viewed in colour.

based on a mass density function that describes the evolution of a curve. This is a different view from the classical GVF strategies, using one of the fundamental theories in physics.

The deformation of a region of interest can be considered as a map T_+: $\Omega \rightarrow \mathcal{R}^2$ with a continuously differentiable inverse T_-. Let the mass density function of the region, surrounded by a continuous contour, be ρ. The mass of the region is given as follows:

$$m_\omega = \int_\omega dT_+ \rho(T_+, t), \tag{5}$$

where m is the mass in the range ω at time t.

Using the dynamical version T_{+0}, ρ_0 and ω_0 of the parameters T_+ respectively, ρ and ω, the right-hand side of Eq. (5) can be decomposed as follows [41]:

$$\begin{aligned} \int_{\omega_0} dT_{+0} \rho_0(T_{+0}) \quad &= \quad \int_{\omega_0} dT_{+0} det(\bigtriangledown T_+(T_{+0}, t)) \\ & \quad \rho(T_+(T_{+0}, t), t), \end{aligned} \tag{6}$$

where the mass density function has an alternative form:

$$\rho(T_+, t) = det(\bigtriangledown \rho_0(q(T_+, t))). \tag{7}$$

Here, q is the inverse transform depending on the deformation map T_+. For simplicity, we use a time-series function to describe the mass:

$$Q(t) = \int_{\omega_0} dT_{+0} det(\bigtriangledown T_+(T_{+0}, t))\rho(T_+(T_{+0}, t), t). \tag{8}$$

We understand that the surrounding contour cannot stop evolving until an energy cost function has been satisfied. Therefore, we expect to find out in what circumstance the contour can be settled. In a noise-free image (almost impossible though), we are able to stop the evolution of the contour if the following condition is met [41]:

$$\frac{\partial Q(t)}{\partial t} = 0. \tag{9}$$

Using Eq. (8), we have the following form, omitting the intermediate derivation:

$$\begin{aligned} \frac{\partial Q(t)}{\partial t} &= \int_{\omega_0} dT_{+0} det(\bigtriangledown T_+(T_{+0}, t))\Big(\frac{\partial}{\partial t}\rho(T_+(T_{+0}, t), t) \\ &\quad +(\bigtriangledown \cdot J)\rho(T_+(T_{+0}, t), t)\Big). \end{aligned} \tag{10}$$

In spite of its complexity, Eq. (10) delineates the progressive characteristics of the contour during its evolution. In other words, the right hand side of Eq. (10) must be of a global minimum absolute value when the contour actually stops moving. For simplicity, we here discuss about the case where $(\bigtriangledown \cdot J)\rho$ is positive definite, which is a common case in practice. As a result, the following inequality holds:

$$\frac{\partial \rho}{\partial t} + (\bigtriangledown \cdot J)\rho \geq \frac{\partial \rho}{\partial t}, \tag{11}$$

where J is a spatial velocity field that denotes the motion vector of the image points on the contour at time t with the following form:

$$J(T_+, t) = \frac{\partial T_+}{\partial t}(q(T_+, t), t). \tag{12}$$

Let T_{+0} be a vector with non-negative components. Combining Eqs. (11) and (12) leads to:

$$\frac{\partial Q(t)}{\partial t} \geq \int_{\omega_0} dT_{+0} det(\bigtriangledown T_+(T_{+0}, t))\frac{\partial \rho}{\partial t}(T_+(T_{+0}, t), t). \tag{13}$$

If the Snake settles on the correct boundary, both constraints Eqs. (2) and (9) must be satisfied at the same time. To jointly satisfy these two constraints in a single objective function, we consider applying the Lagrange multiplier rule [42]. This approach has the advantage of using one of the constraints as a regularisation term when the other is pursued. In other words, we seek an optimal value for the parameter $\lambda \in \mathcal{R}$ such that:

$$\begin{aligned} \Big[\frac{\partial}{\partial s}\Big(\alpha\frac{\partial \mathbf{x}}{\partial s}\Big) - \frac{\partial^2}{\partial s^2}\Big(\beta\frac{\partial^2 \mathbf{x}}{\partial s^2}\Big) - \bigtriangledown E_{ext}(\mathbf{x})\Big] \\ -\lambda\Big[\int_{\omega_0} dT_{+0} det(\bigtriangledown T_+(T_{+0},t)) \\ \Big(\frac{\partial}{\partial t}\rho(T_+(T_{+0},t),t) + (\bigtriangledown\cdot J)\rho(T_+(T_{+0},t),t)\Big)\Big] \\ = \quad 0. \end{aligned} \tag{14}$$

Let the first term of the left-hand side of Eq. (14) be F_{T_1} and the second term F_{T_2}. In our case, the curve $\mathbf{x}$ in F_{T_1} is closely related to the map function T_+ in F_{T_1}. In fact, the latter determines the location of $\mathbf{x}$ in the image, and any change of T_+ subsequently causes variations of $\mathbf{x}$. In the meantime, the Lagrange multiplier λ can be updated as

$$\lambda = \inf_{\mathbf{s}\in[0,1], T_{+0}\in\omega_0} \frac{F_{T_1}}{F_{T_2}}, \tag{15}$$

where the conditions of $\mathbf{s}$ and T_{+0} must be jointly satisfied. Substituting Eq. (11) to (14), we have the following form:

$$\begin{aligned} \Big[\frac{\partial}{\partial s}\Big(\alpha\frac{\partial \mathbf{x}}{\partial s}\Big) - \frac{\partial^2}{\partial s^2}\Big(\beta\frac{\partial^2 \mathbf{x}}{\partial s^2}\Big) - \bigtriangledown E_{ext}(\mathbf{x})\Big] - \\ \lambda\Big[\int_{\omega_0} dT_{+0} det(\bigtriangledown T_+(T_{+0},t))\Big(\frac{\partial}{\partial t}\rho(T_+(T_{+0},t),t)\Big)\Big] \geq \quad 0. \end{aligned} \tag{16}$$

Let the left-hand side of Eq. (16) be $\mathcal{L}(t)$. Thus, we can re-write Eq. (16) according to [43]: $\Phi(t) = \mathcal{L}^T\mathcal{L} = \| \mathcal{L} \|^2$. Eventually, the numerical solution of Eq. (16) satisfies the following condition:

$$\min \Phi(t) = \min(\|\mathcal{L}\|^2). \tag{17}$$

Using such a combinatorial way (i.e. Eq. (16)) helps handling the segmentation problem in noisy images. This will be justified in the experimental section. However, seeking such a minimisation as Eq. (17) is non-trivial. First of all, compromising both the partial differential equation (PDE) and

the mass function of a region during the contour evolution is not easy to achieve due to the different objectives. Secondly, an analytical solution to the PDE problem is extremely difficult to obtain as there are no prior information or boundary conditions to use. A fast and optimal solution to Eq. (17) is therefore pursued in the next subsection.

2.3. Simplified solution to the segmentation problem

To obtain an optimal solution to Eq. (16), we first investigate the two terms of the left hand side of Eq. (16), and seek corresponding solutions for individual local energy minimisations. These two different operations are intersectionally applied to the two energy terms before a global minimum is found. According to [22], the gradient vector flow field is defined as the vector field $\mathbf{v}(x, y)$ that minimises the following energy functional: $\mathcal{E} = \int\int \mu(u_x^2 + u_y^2 + v_x^2 + v_y^2) + |\bigtriangledown f|^2|\mathbf{v} - \bigtriangledown f|^2 dxdy$, where $\mathbf{v}(x, y) = [u(x, y), v(x, y)]$. The solution to this minimisation is

$$\begin{cases} \mu\bigtriangledown^2 u - (u - f_x)(f_x^2 + f_y^2) = 0 \\ \mu\bigtriangledown^2 v - (v - f_y)(f_x^2 + f_y^2) = 0 \end{cases} \tag{18}$$

where $\bigtriangledown^2$ is the Laplacian operator. Taking a closer look at the second term of the left-hand side of Eq. (16), we have:

$$det(\bigtriangledown T_+(T_{+0}, t)) = \Pi_r eig(\bigtriangledown T_+(T_{+0}, t)), \tag{19}$$

where r is the dimension and eig denotes the eigenvalues of $\bigtriangledown T_+(T_{+0}, t)$. The derivative $\bigtriangledown T_+(T_{+0}, t)$ can be approximated to be the difference of two neighbouring deformable shapes against the time interval:

$$\bigtriangledown T_+(T_{+0}, t) \approx \frac{T_+(T_{+0}, t) - T_+(T_{+0}, t - \triangle T)}{\triangle T}, \tag{20}$$

where the initial state of $\bigtriangledown T_+(T_{+0}, t)$ is null and $\triangle T$ is the image sampling interval (a constant in this case).

Now, we look at the parameterisation of ρ. The Euclidean distance between the centre of the mass and each point j on the image is represented as $d((x_j, y_j), t)$. Similarly, the Euclidean distance between the centre of the region and each point i on the contour is $D(x_i, y_i)$. Therefore, the mass density ρ is computed as follows:

$$\rho(T_+(T_{+0}, t), t) = \frac{\int_j d((x_j, y_j), t)}{D(x_i, y_i)}. \tag{21}$$

Thus, we have:

$$\frac{\partial \rho}{\partial t}(T_+(T_{+0},t),t) = \frac{\partial(\int_j d((x_j,y_j),t))}{D(x_i,y_i)\partial t} \approx \frac{\alpha \bar{d}(t)}{D(x_i,y_i)}, \tag{22}$$

where α is a constant based on empirical results, and $\bar{d}(t)$ is the average moving distance of the centre of the mass over a short period. Eq. (22) shows that the variation of mass density ρ is proportional to the motion distance of the mass centre.

We now attempt to work out an efficient technique in order to obtain an optimal numerical solution to Eq. (22). Techniques such as image moments [44, 45], level sets [15], wavelets [46] or stochastic analysis [47] can be used to handle this problem in different circumstances. Most of these approaches require the objective functions to be parameterised. Moreover, these methods require significant computation efforts before convergence is reached. In our approach, which is significantly different from the classical approaches, we use a mean shift based algorithm that can achieve fast similarity search by examining the intensity distributions over two neighboring iterations [48].

It is worth pointing out that the proposed algorithm significantly differs from the classical approaches such as [24, 35, 38, 39] in the sense that the convergence of the proposed algorithm relies upon the intensity histogram of the region outlined by the contour, the distance between each point within the region outlined by the contour and its mass centre and the distance between each point of the contour and its centre. However, the approaches presented in [24, 35, 38, 39] only depend on the distance between each point of the contour and its centre. Evidence shows that the proposed algorithm leads to better performance than the others due to the joint action of the regional contents and the distances as mentioned.

2.4. Mean shift for contour evolution

Fig. 3 shows two exemplar images with corresponding intensity histograms and final segmentation results (the boundaries are shown in green colour). The mean shift analysis used in the energy minimisation is to enhance the discrimination capability of image pixels. Let $K(\phi)$ be a kernel and $f(\phi)$ be a multivariate kernel density estimation of the intensity values within the region outlined by the evolving contour (ϕ refers to the image points). Then,

$$f(\phi) = \frac{1}{n}\sum_{i=1}^{n} K_H(\phi - \phi_i), \tag{23}$$

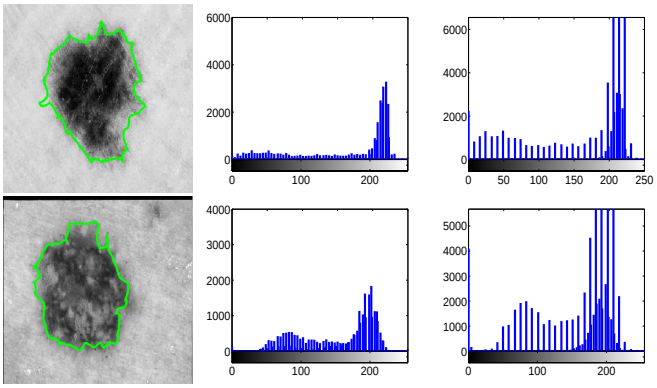

(a) (b) (c)

Figure 3: Interaction of neighbouring pixels in image segmentation: (a) Original images superimposed by the segmentation contour, (b) intensity histogram of the regions outlined by the contour (indicated by green colour), and (c) intensity histogram of the regions outside the contour. Better viewed in colour.

where ϕ_i indicate the neighboring points, and $K_H(\phi) = |H|^{-\frac{1}{2}} K(H^{-\frac{1}{2}}\phi)$, where H is a symmetric positive definite $(l \times l)$ bandwidth matrix and n is the number of image points. In a real application, the bandwidth matrix H can be diagonal $H = diag[h_1^2, ..., h_l^2]$, or proportional to the identity matrix $H = h^2 I$. Thus, we have $f(\phi) = \frac{1}{nh^l} \sum_{i=1}^{K} \left(\frac{\phi - \phi_i}{h} \right)$. We can use a radially symmetrical kernel that satisfies $K(\phi) = C_{k,l} k(\| \phi \|^2)$, where $C_{k,l}$ is a normalised constant that enables $K(\phi)$ to be integrated to 1. As a result,

$$f_{h,k}(\phi) = \frac{C_{k,l}}{nh^l} \sum k\Big(\Big\| \frac{\phi - \phi_i}{h} \Big\|^2 \Big). \tag{24}$$

When the Snake settles, the intensity histograms over two neighboring iterations will be similar. If this occurs, the Snake possibly stops moving, resulting in unchanged density estimations in this circumstance: $\bigtriangledown f(\phi) = 0$. Therefore, $\bigtriangledown f(\phi) = \frac{2C_{k,l}}{nh^{l+2}} \sum (\phi - \phi_i) k'\Big(\Big\| \frac{\phi - \phi_i}{h} \Big\|^2 \Big) = 0$. Introducing

$G(\phi) = -k'(\phi)$, we have:

$$\begin{aligned}
\bigtriangledown f(\phi) &= \frac{2C_{k,l}}{nh^{l+2}} \sum (\phi - \phi_i) G\Big(\Big\| \frac{\phi - \phi_i}{h} \Big\|^2 \Big) \\
&= \frac{2C_{k,l}}{nh^{l+2}} \left[\sum_{i=1}^{n} G\Big(\Big\| \frac{\phi - \phi_i}{h} \Big\|^2 \Big) \right] \cdot \\
&\quad \left[\frac{\sum_{i=1}^{n} \phi_i G\Big(\Big\| \frac{\phi - \phi_i}{h} \Big\|^2 \Big)}{\sum_{i=1}^{n} G\Big(\Big\| \frac{\phi - \phi_i}{h} \Big\|^2 \Big)} - \phi \right] \\
&= 0. \qquad (25)
\end{aligned}$$

The mean shift is the last term of the right-hand side of Eq. (25), which can be further simplified as follows:

$$m_{h,G}(\phi) = \frac{1}{2} h^2 C \frac{\bigtriangledown f_{h,k}(\phi)}{f_{h,G}(\phi)}, \qquad (26)$$

where $f_{h,G}(\phi)$ has a similar form to that of Eq. (24) but uses G instead of h. Referring to Eq. (22), we have

$$m_{h,G}(\phi) \approx c_k \bar{d}(t), \qquad (27)$$

which indicates that the minimisation of mean shift is also equivalent to the minimisation of the mass density function of Eq. (22) (c_k is a scalar). This mean shift procedure determines the grouping of the image points in the whole image domain, whilst having the benefit of efficiently reaching the convergence. Mean shift is parameter-free and its kernel can be modified so as to adapt to different applications. Consequently, when implementing Eq. (16), we include the computation of mean shift during each iteration for the region surrounded by the evolving boundary.

Fig. 4 illustrates that, as the iteration proceeds, the GVF, a non-conservative force based on the Helmholtz theorem, successfully approximates boundary concavities and is capable of topological transformation in a certain way. We also observe that the intensity histograms of the region outlined by the evolving contour become stabilised after a number of iterations. The mean shift will reach a minimisation that is evolutionarily stable, which affects the settlement of the Snake through the varied λ (see Eq. 15). Without this mean shift term for the regularisation purpose, the GVF would drive the Snake to continuously shrink and cause over-segmentation in this particular example.

Algorithm 1 Proposed mean shift based GVF image segmentation (MS-GVF) algorithm.

1: Initialise the contour and the corresponding parameters
2: **for** Iterations i = 1:m (m is normally larger than 500) **do**
3: Employ the classical Snake (i.e. Eq. (2)).
4: Compute the mean of the intensity histogram of each region surrounded by the evolving contour.
5: Obtain the difference of the two means in two neighboring iterations.
6: Introduce the above difference into Eq. (22).
7: Substitute Eqs. (19)-(22) and (26) into Eq. (16).
8: Calculate λ using Eq. (15).
9: Evaluate the left hand side of Eq. (16) for the differences over two consecutive iterations.
10: Iterate steps 3-9 until Eq. (17) is satisfied or the difference between two consecutive iterations < 0.001.
11: **end for**

2.5. Convergence analysis

The proposed Mean Shift based GVF algorithm is shown in Algorithm 1. Looking at the energy function shown in Eq. (16), even though one of the two functionals converges, Eq. (16) can still be further optimised for a better settlement. The convergence properties of the energy function therefore can be divided into two parts.

First, we examine the case of mean shift. Assume that $S \subseteq \mathcal{R}^d$, $\bigtriangledown f_{h,k} : S \to \mathcal{R}$ and have continuous derivatives of 2nd order. $\forall \eta_t \in S$ and $\bigtriangledown^2 F_{h,k}(\eta_t)$ $(t = 1, 2, ...)$ is a negative definite matrix. $F_{h,k}(\eta_t)$ can be expanded using the Taylor series theorem given $\eta = \eta_t + \xi_t d_t \in S$:

$$F_{h,k}(\eta_t + \xi_t d_t) = F_{h,k}(\eta_t) + \xi_t \bigtriangledown F_{h,k}(\eta_t + \theta \xi_t d_t)^T, \tag{28}$$

where $0 < \theta < 1$. Let $\varphi(\theta) = \lambda_t \bigtriangledown F_{h,k}(\eta_t + \theta \xi_t d_t)^T d_t$. We then have [49]: $\lim_{\theta \to 0} \varphi(\theta) = \xi_t \bigtriangledown F_{h,k}(\eta_{t+1})^T \bigtriangledown F_{h,k}(\eta_t) > 0$. The derivative of $\varphi(\theta)$ is $\varphi'(\theta) = (\eta_{t+1} - \eta_t)^T \bigtriangledown^2 F_{h,k}(\eta_t + \theta \xi_t d_t)^T (\eta_{t+1} - \eta_t) < 0$. Therefore, $\varphi(\theta)$ is monotonically decreasing, $\forall \theta(0, 1)$. This leads to $F_{h,k}(\eta_{t+1}) > F_{h,k}(\eta_t)$. Hence, $F_{h,k}(\eta_t)$ is strictly monotonically increasing and convergent, resulting in $\lim_{F_{h,k} \to F_{h,k}(\bar{\eta})} = 0$, where $\bar{\eta} \in S$ [49].

Second, we investigate the convergence of the left hand side of Eq. (16), assuming that mean shift has reached its minimisation after a certain num-

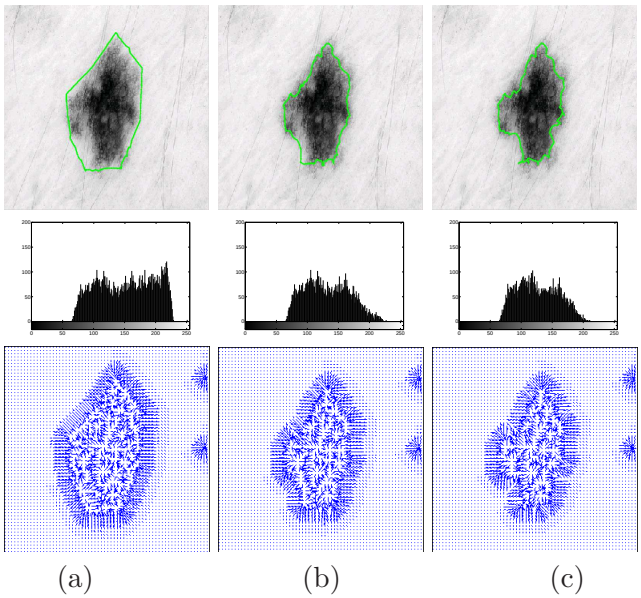

Figure 4: Intensity histograms (row 2) and GVF field maps (row 3) of the regions outlined by the contour (row 1: green colour) in different iterations: (a) 5-th, (b) 25-th, and (d) 40-th. The parameters used in this example are $\alpha = 0.1$, $\beta = 0.01$, $\gamma = 1$, $\kappa = 0.6$. Better viewed in colour.

ber of iterations. Referring to [50], one has

$$\begin{aligned} \mathcal{L}(\mathbf{u}+\mathbf{v}) - \mathcal{L}(\mathbf{v}) &= [\mu|\bigtriangledown \mathbf{u}|^2 + 2\mu \bigtriangledown \mathbf{v} \cdot \bigtriangledown \mathbf{u} + |\bigtriangledown f|^2 \\ &\quad |\mathbf{u}|^2 + 2|\bigtriangledown f|^2(\mathbf{v} - \bigtriangledown f) \cdot \mathbf{u}] + \upsilon, \end{aligned} \tag{29}$$

where $\mathbf{v} + \mathbf{u} \in S$ and $\upsilon \to 0$ due to the slight variation in the mean shift iteration. Given the Gâteaux variation of the functional as $\epsilon\mathcal{L}(\mathbf{v};\mathbf{u}) = \lim_{\rho \to 0} \frac{\mathcal{L}(\mathbf{v}+\delta\mathbf{u}) - \mathcal{L}(\mathbf{v})}{\rho}$, we then have: $\mathcal{L}(\mathbf{v}+\mathbf{u}) - \mathcal{L}(\mathbf{v}) - \epsilon\mathcal{L}(\mathbf{v};\mathbf{u}) = \mu|\bigtriangledown \mathbf{u}|^2 + |\bigtriangledown f|^2|\mathbf{u}|^2 + \upsilon \geq 0$, which indicates that the left hand side of Eq. (16) is convex.

3. Experimental work

To fully evaluate our proposed MSGVF algorithm in terms of the initialisation invariance and convergence accuracy we use a set of 100 dermoscopic images (30 invasive malignant melanoma and 70 benign) obtained from the

EDRA Interactive Atlas of Dermoscopy [51] and the dermatology practices of Dr. Ashfaq Marghoob (New York, NY), Dr. Harold Rabinovitz (Plantation, FL) and Dr. Scott Menzies (Sydney, Australia). The benign lesions include nevocellular nevi and dysplastic nevi. Manual borders were obtained by selecting a number of points on the lesion border, connecting these with a 2nd-order B-spline and finally filling the resulting closed curve. Three sets of manual borders were determined by expert dermatologists and serve as a ground truth for the experiments.

In addition, the algorithm was evaluated on a set of 40 retinal images obtained from the DRIVE database [52]. These images have been randomly selected from a screening database of 400 diabetic subjects aged 25-90. 33 of the images do not show any sign of diabetic retinopathy while in 7 signs of mild diabetic retinopathy are apparent. Each image is a true colour image of 768 by 584 pixels. The field of view of each image is circular with a diameter of approximately 540 pixels.

In our current implementation, the color dermoscopic images are converted to grayscale using the CCIR 601 standard (Luminance = $0.2989 * \text{Red} + 0.5870 * \text{Green} + 0.1140 * \text{Blue}$). Colour information may be used in the future to improve the results. In the experimental evaluation, we used a PC with Intel(R) Core(TM)2 CPU (2.66 GHz) and 2 GB RAM. The algorithms we compare are the classical GVF algorithm [22], level set segmentation [10] (LS), mean shift constrained GVF (MGVF) [24, 38, 39] and the proposed MSGVF algorithm. For the two GVF based methods, the parameters have been set to: α (tension of the Snake) = 0.05, β (rigidity of the Snake) = 0.0, γ (step size in one iteration) = 1.0, and κ (external force weight) = 0.6. These parameters have been chosen due to their best resulting outcomes from these specific datasets.

3.1. Dermoscopic images

In this sub-task, the evaluation consists of four parts. First, the four algorithms are evaluated using the dermoscopic images where the lesion areas possess smooth and clear edges. This is the easiest case in the evaluation. Second, the performance of the overall algorithms is investigated in the presence of irregular edges in the lesion regions. This examination will bring certain challenges in terms of the algorithms' capability in these "noisy" environments. Third, we examine how these schemes perform if the edges of the lesion areas look ambiguous. This test is more rigorous than the above tests in the way that a segmentation algorithm needs to effectively locate a vague boundary before the segmentation procedure starts. Finally,

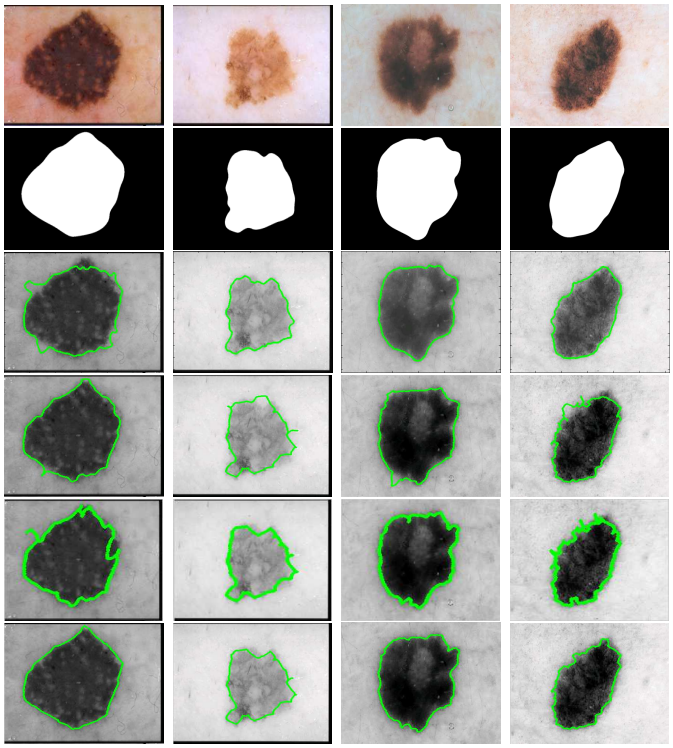

Figure 5: Segmentation results of dermoscopic images with smooth and clear lesion edges. Row 1: original images; Row 2: ground truth; Row 3: level set; Row 4: classical GVF; Row 5: MGVF; Row 6: MSGVF. Better viewed in colour.

we evaluate the performance of the different algorithms (i.e. GVF, MSGVF and level set) using changed initial contours.

In the first test, the various algorithms are evaluated in the presence of smooth and clear edges. Image examples of the experimental results are illustrated in Fig. 5. In general, the algorithms obtain similar outcomes. However, taking a closer look, we can observe that the proposed MSGVF algorithm has a better fit to the ground truth than the classical GVF method. For example, the 2-nd and 3-rd columns of Fig. 5 illustrate that the classical GVF algorithm leads to worse settlements, compared to the proposed MSGVF algorithm. Also, it can be noticed that the level set algorithm causes a significantly misplaced boundary on the first image of Fig. 5.

In the second test, the lesion edges have irregular shapes that make accurate segmentation more difficult as the energy functions used in the iterations of these algorithms have to make more effort to handle various saddle points in the optimisation. Exemplar results for this group of images are presented in Fig. 6. We observe that MSGVF has the most consistent outcomes compared to the other methods. The classical GVF technique leads to some spikes on the final settlements as the evolution of the contour struggles to capture the curvatures. For columns 2 and 3, it is clear that the level set and MGVF methods exhibit difficulties in handling concave shapes. In contrast, the proposed MSGVF algorithm is successful in driving the contour to follow these shapes.

In the third test group, the skin images have ambiguous edges where a segmentation algorithm needs to "define" a more clear boundary in the first instance. Examples of this group are illustrated in Fig. 7, together with the obtained segmentations. The classical GVF algorithm leads to local convergence and numerous spikes along the final contours. Columns 1 and 4 of the level set method show that this approach is not successful in capturing the geometric deformation in the images, compared to the proposed MSGVF algorithm.

Finally, we investigate the case where the starting contours are changed before segmentation is performed. Two sample images are given in Fig. 8. It is observed that the proposed MSGVF algorithm has the most consistent and accurate segmentation results, whereas the other two methods lack this consistency, leading to failed converge onto the correct boundaries.

As ground truth information is available for the complete dermoscopic image set, we can also evaluate the various algorithms in a quantitative form. For each image segmentation we record the number of True Positives TP (the number of pixels that were classified both by the algorithm and the expert as lesion pixels), True Negatives TN (the number of pixels that were

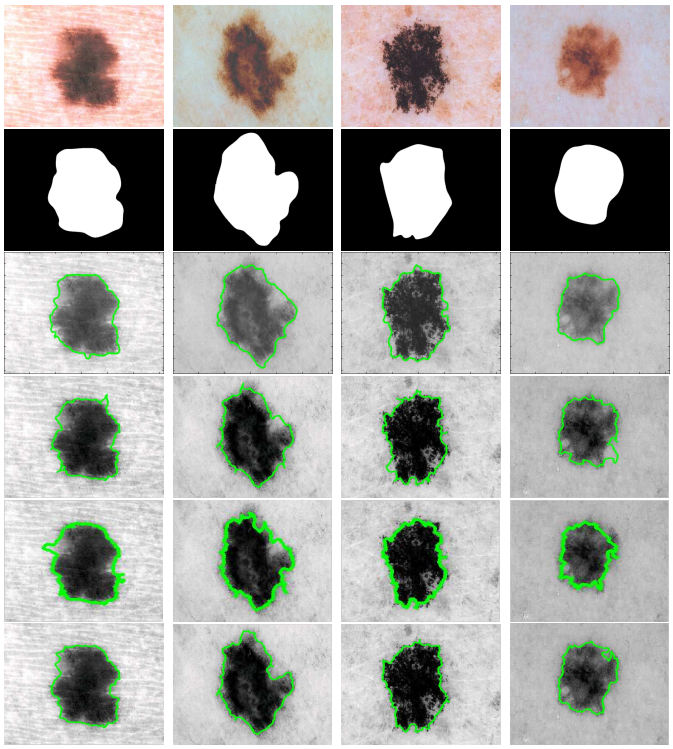

Figure 6: Segmentation results of dermoscopic images with irregular lesion edges. Row 1: original images; Row 2: ground truth; Row 3: level set; Row 4: classical GVF; Row 5: MGVF; Row 6: MSGVF. Better viewed in colour.

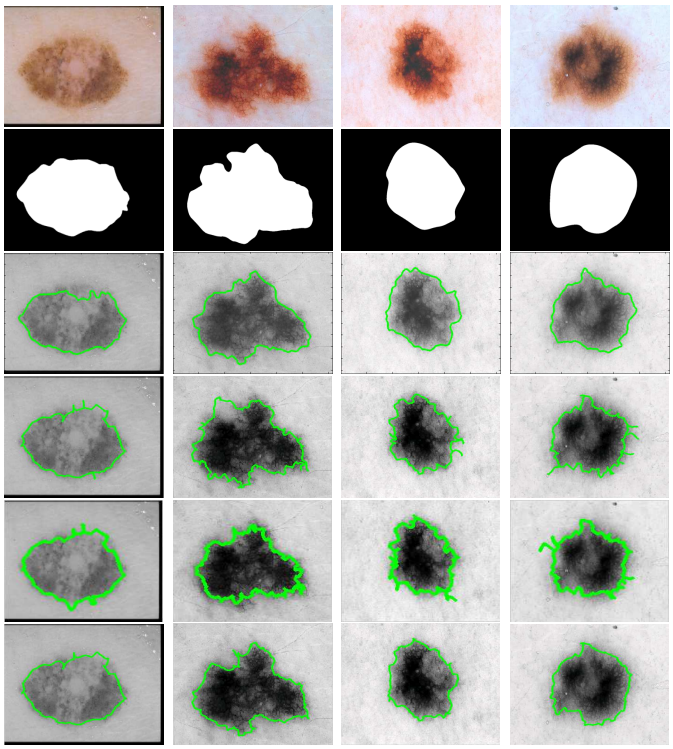

Figure 7: Segmentation results of example dermoscopic images with ambiguous lesion edges. Row 1: original images; Row 2: ground truth; Row 3: level set; Row 4: classical GVF; Row 5: MGVF; Row 6: MSGVF. Better viewed in colour.

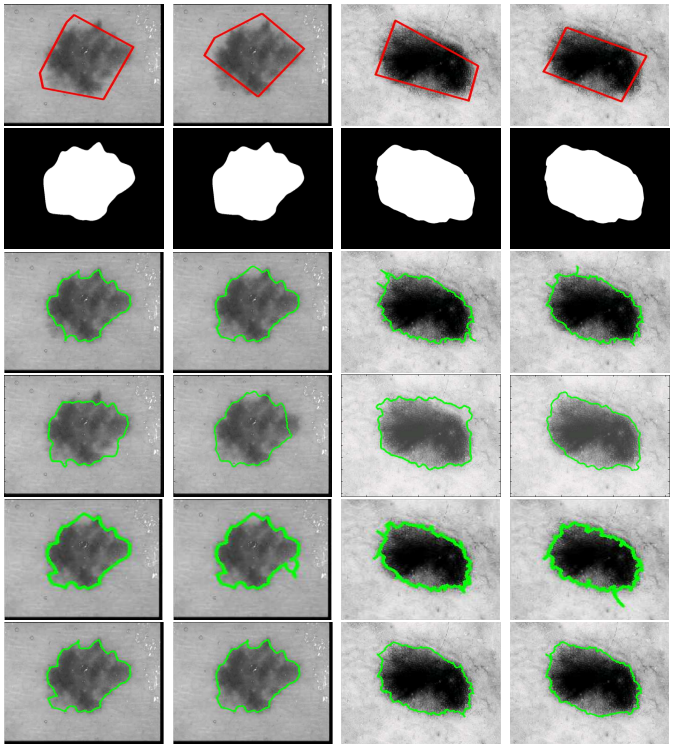

Figure 8: Segmentation results of example dermoscopic images with different starting contours. Row 1: original images superimposed by starting contours; Row 2: ground truth; Row 3: GVF; Row 4: level set; Row 5: MGVF; Row 6: MSGVF. Better viewed in colour.

Table 1: Segmentation performance with reference to Figs. 5-7.
For each algorithm the median sensitivity/specificity are given.

Algorithms	Fig. 5	Fig. 6	Fig. 7
classical GVF	0.75/0.95	0.71/0.99	0.66/0.99
level sets	0.79/0.96	0.74/0.99	0.73/0.91
MGVF	0.80/0.98	0.78/0.99	0.75/0.94
MSGVF	0.84/0.97	0.80/1.00	0.77/0.93

classified both by the algorithm and the experts as non-lesion pixels), False Positives FP (the number of instances where a non-lesion pixel was falsely classified as part of a lesion by an algorithm) and False Negatives FN (the number of instances where lesion pixels were falsely classified as non-lesion by an algorithm). From this we can then calculate the sensitivity SE (or true positive rate): $SE = \frac{TP}{TP+FN}$ and the specificity SP (or true negative rate): $SP = \frac{TN}{TN+FP}$.

Table 1 gives the sensitivity and specificity obtained by all algorithms over the image examples shown on Figs. 5-7 and compared to all three ground truth segmentations (median SE and SP based on all three manual segmentations are reported). It is observed that the proposed MSGVF has the highest sensitivity and specificity values, indicating the best segmentation capability. In Table 2 we show the sensitivity and specificity obtained by all algorithms over the entire dermoscopic database and compared to all three ground truth segmentations (median SE and SP based on all three manual segmentations are reported). It can be seen that the proposed MSGVF performs significantly better with an median sensitivity of 86% while the other algorithms achieve a sensitivity of less than 81%. In addition, MSGVF sustains more consistent results as indicated by the lowest standard deviations of both sensitivity and specificity. As specificity is fairly similar for all algorithms, we can conclude that MSGVF provides the best segmentation on the given dataset.

3.2. Optic disc images

We perform the evaluation on this dataset in two parts. First, the classical GVF, level set segmentation and our proposed MSGVF algorithms are evaluated using the retinal images where the optic disc (OD) is clearly visible from the observer's point of view which represents the simplest case in our evaluation. In addition, the performance of the algorithms is investigated in the presence of vague optic discs in the retinal images. These examinations allow the algorithms to be fully evaluated in different noisy environments.

Table 2: Segmentation performance with reference to the complete dermoscopic dataset. For each algorithms the median sensitivity and specificity are given. Values in brackets indicate standard deviations of the measures.

Algorithms	Sensitivity	Specificity
classical GVF	0.74(0.13)	0.99(0.10)
level sets	0.76(0.09)	0.99(0.07)
MGVF	0.81(0.09)	0.99(0.08)
MSGVF	0.86(0.07)	0.99(0.05)

Second, we examine how the algorithms perform if the initial contours are varied. This is a rigorous test that fails a segmentation algorithm if it does not work in a consistent and stable manner.

Examples of the first test are illustrated in Fig. 9. As can be seen, for all these images, the proposed MSGVF algorithm provides consistently accurate results compared to the other two algorithms. This can be attributed to the computation of mean fields in the domain of the proposed approach, which dynamically balances internal and external energy forces during the contour evolution. The poor performance of the classical GVF, MGVF and level set algorithms is due to the distraction of the blood vessels nearby the optic disc.

One of the main challenges in image segmentation is whether or not the performance of a segmentation algorithm can be kept consistent for different initialisation circumstances. To validate this, we randomly specify the starting contours for the involved images. This is followed by the regular routine of the algorithms. Fig. 10 demonstrates that despite varied initial contour position, the resultant segmentation borders are visually indistinguishable. When the initial contour is relatively far from the actual one, three approaches obtain similar segmentation results but it is clear that the proposed MSGVF algorithm has more consistent outcomes than the other algorithms.

Table 3 illustrates that the proposed MSGVF algorithm has the best specificity and sensitivity, compared to the other algorithms. It is worthy to point out that MGVF and level sets approaches lead to similar sensitivity results, both of which are better than that of the classical GVF. It is also observed that all of the tested algorithms share approximately the same specificity results (0.99-1.00). This indicates that all of them correctly exclude the areas that do not belong to the real regions of interest. To better measure the similarity between a segmented region and the ground truth, especially in the presence of a small segmentation area, we here apply

Table 3: Segmentation performance with reference to the complete optic disc dataset.

Algorithms	Sensitivity	Specificity	XOR
classical GVF	0.70(0.06)	0.99(0.04)	0.45(0.13)
level sets	0.72(0.07)	0.99(0.01)	0.39(0.11)
MGVF	0.74(0.09)	0.99(0.03)	0.37(0.09)
MSGVF	0.78(0.04)	1.00(0.0)	0.33(0.09)

Table 4: Comparisons of time consumption of each algorithm for a single image. Units: seconds.

	classical GVF	level sets	MGVF	MSGVF
Time	16	14	17	22

an XOR operation. This XOR operation is defined as a ratio between the non-overlapped area and the size of the ground truthed segmentation region. The smaller XOR value is, the higher similarity between the segmentation and the ground truth is achieved. The last column of Table 3 shows that the proposed MSGVF algorithm has the least dissimilarity.

4. Conclusions and future work

In this paper we have presented a novel variational framework for image segmentation. Both the accuracy and robustness of the proposed MSGVF algorithm have been validated against competing approaches including classical GVF and level set. Unlike these state-of-the-art techniques, the proposed method is fairly accurate as it obtains an optimal solution during the iterations for energy minimisation. The proposed algorithm integrates the classical GVF term with a mass density function. The final solution towards this integrated functional is based on a numerical optimisation procedure with the support of mean shift estimation.

The main drawback of the proposed algorithm is that it involves a large amount of computation to achieve convergence. While it has been shown that numerical convergence of the evolving contour is guaranteed, the solution-rendering process is rather time consuming. An example of time consumption of different algorithms for a single image is illustrated in Table 4. Therefore, future work is directed towards reducing the complexity of the computation by optimising the implementation whilst using gradient descent methods.

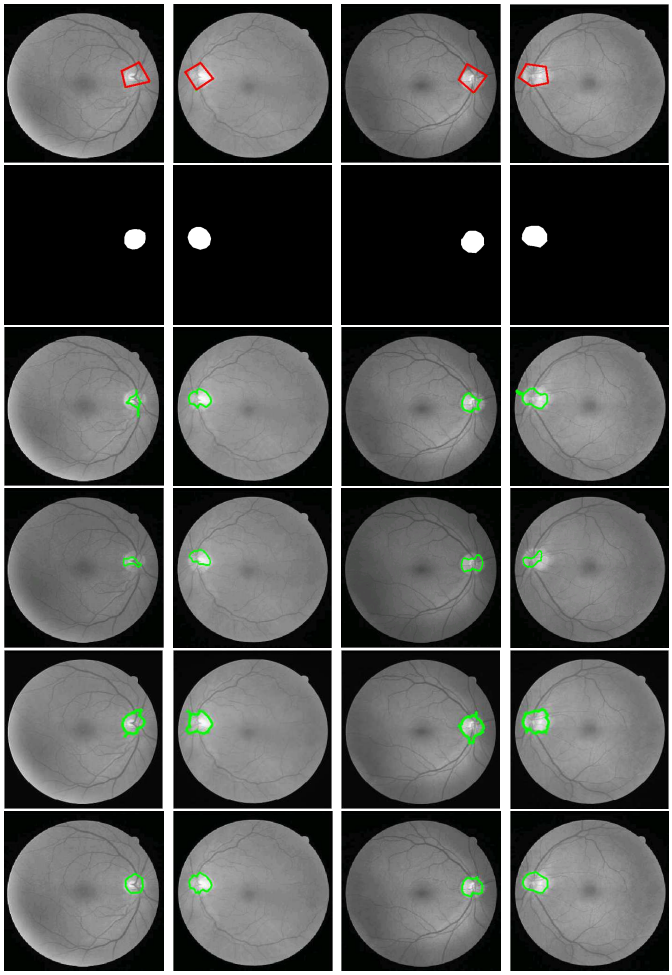

Figure 9: Segmentation results of optic disc images. Row 1: original images superimposed by starting contours; Row 2: ground truth; Row 3: classical GVF; Row 4: level set; Row 5: MGVF; Row 6: MSGVF. Better viewed in colour.

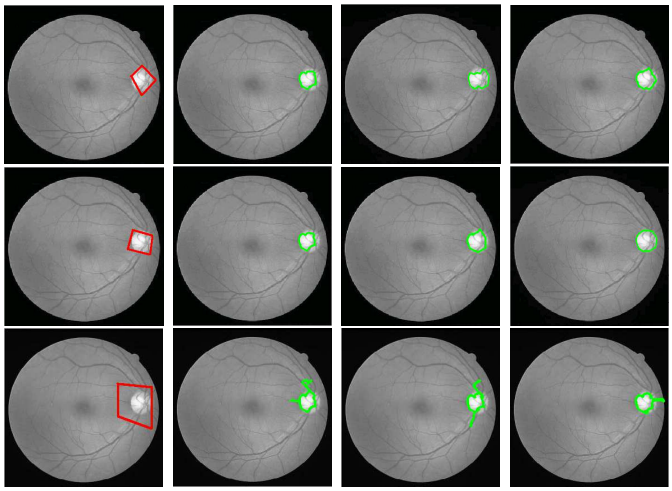

Figure 10: Segmentation results with different initial contours of optic disc. Column 1: original images superimposed by starting contours; Column 2: classical GVF; Column 3: level set; Column 4: MSGVF. Better viewed in colour.

Acknowledgments

The assistance of William V. Stoecker, Joseph M. Malters, James M Grichnik, Kathy Clawson, Jiali Shen and Mohsen Abbas Pour Seyyedi in obtaining the manual borders for the two image datasets is gratefully acknowledged. The work of X. Li is supported by the National Basic Research Program of China (973 Program) (Grant No. 2012CB316400) and the National Natural Science Foundation of China (Grant No. 61125106).

References

[1] M. Kass, A. Witkin, D. Terzopoulos, Snakes: Active contour models, in: Proc. of the International Conference on Computer Vision, 1987, pp. 259–268.

[2] B. Wang, X. Gao, D. Tao, X. Li, A unified tensor level set for image segmentation, IEEE Trans. Sys. Man Cyber. Part B 40 (3) (2010) 857–867.

[3] S. Zhu, A. Yuille, Region competition: Unifying snakes, region growing, and bayes/mdl for multiband image segmentation, IEEE Transactions on Pattern Analysis and Machine Intelligence 18 (9) (1996) 884–900.

[4] Y. Du, E. Arslanturk, Z. Zhou, C. Belcher, Video-based noncooperative iris image segmentation, IEEE Transactions on Systems, Man, and Cybernetics, Part B 41 (1) (2011) 64–74.

[5] X. Gao, B. Wang, D. Tao, X. Li, A relay level set method for automatic image segmentation, IEEE Transactions on Systems, Man, and Cybernetics, Part B 41 (2) (2011) 518–525.

[6] X. Han, C. Xu, J. Prince, A topology preserving level set method for geometric deformable models, IEEE Transactions on Pattern Analysis and Machine Intelligence 25 (2003) 755–768.

[7] J. Stahl, S. Wang, Globally optimal grouping for symmetric closed boundaries by combining boundary and region information, IEEE Trans. Pattern Anal. Mach. Intell. 30 (3) (2008) 395–411.

[8] I. Ayed, S. Li, I. Ross, A statistical overlap prior for variational image segmentation, International Journal of Computer Vision 85 (1) (2009) 115–132.

[9] L. Cohen, R. Kimmel, Global minimum for active contour models: A minimal path approach, International Journal of Computer Vision 24 (1) (1997) 57–78.

[10] C. Li, J. Liu, M. Fox, Segmentation of edge preserving gradient vector flow: An approach toward automatically initializing and splitting of snakes, in: IEEE Conference on Computer Vision and Pattern Recognition, 2005, pp. 162–167.

[11] D. Mumford, J. Shah, Optimal approximations by piecewise smooth functions and associated variational problems, Communications on Pure and Applied Mathematics 42 (5) (1989) 577–685.

[12] T. Chan, L. Vese, Active contours without edges, IEEE Transactions on Image Proc. 10 (2) (2001) 266–277.

[13] G. Sapiro, A. Tannenbaum, Affine invariant scale-space, International Journal of Computer Vision 11 (1) (1993) 25–44.

[14] V. Caselles, R. Kimmel, G. Sapiro, Geodesic active contours, International Journal of Computer Vision 22 (1) (1997) 61–79.

[15] R. Malladi, J. Sethian, B. Vemuri, Shape modeling with front propagation: A level set approach, IEEE Transactions on Pattern Analysis and Machine Intelligence 17 (2) (1995) 158–175.

[16] S. Osher, J. Sethian, Fronts propagating with curvature dependent speed: Algorithms based on hamilton-jacobi formulations, Journal of Computational Physics 79 (1988) 12–49.

[17] T. McInerney, D. Terzopoulos, T-snakes: topological adaptive snakes, Medical Image Analysis 4 (2) (2000) 73–91.

[18] C. Xu, D. Pham, J. Prince, Handbook of Medical Imaging - Volume 2: Medical Image Processing and Analysis, SPIE Press, Bellingham, WA, 2000, Ch. Medical image segmentation using deformable models, pp. 129–174.

[19] L. Cohen, On active contour models and balloons, CVGIP: Image Understanding 53 (2) (1991) 211–218.

[20] L. Cohen, I. Cohen, Finite element methods for active contour models and balloons for 2d and 3d images, IEEE Transactions on Pattern Analysis and Machine Intelligence 15 (1993) 1131–1147.

[21] D. Cremers, F. Tischhäuser, J. Weickert, C. Schnörr, Diffusion snakes: Introducing statistical shape knowledge into the mumford-shah functional, International Journal of Computer Vision 50 (3) (2002) 295–313.

[22] C. Xu, J. Prince, Snakes, shapes, and gradient vector flow, IEEE Transactions on Image Processing 7 (3) (1998) 359–369.

[23] C. Xu, J. Prince, Generalized gradient vector flow external forces for active contours, Signal Processing 71 (2) (1998) 131–139.

[24] T. Liu, H. Zhou, F. Lin, Y. Pang, J. Wu, Improving image segmentation by gradient vector flow and mean shift, Pattern Recognition Letters 29 (1) (2008) 90–95.

[25] N. Paragios, O. Mellina-Gottardo, V. Ramesh, Gradient vector flow fast geometric active contours, IEEE Transactions on Pattern Analysis and Machine Intelligence 26 (3) (2004) 402–407.

[26] S. Osher, N. Paragios, Geometric Level Set Methods in Imaging,Vision,and Graphics, Springer-Verlag New York, Inc., Secaucus, NJ, USA, 2003.

[27] C.-H. Chuang, W.-N. Lie, A downstream algorithm based on extended gradient vector flow field for object segmentation, IEEE Transactions on Image Processing 13 (10) (2004) 1379–1392.

[28] L. Yang, P. Meer, D. Foran, Unsupervised segmentation based on robust estimation and color active contour models, IEEE Transactions on Information Technology in Biomedicine 9 (3) (2005) 475–486.

[29] A. Vasilevskiy, K. Siddiqi, Flux maximizing geometric flows, IEEE Transactions on Pattern Analysis and Machine Intelligence 24 (12) (2002) 1565–1578.

[30] V. Caselles, R. Kimmel, G. Sapiro, Geodesic active contour, in: IEEE International Conference on Computer Vision, 1995, pp. 694–699.

[31] J. Tang, S. Acton, Vessel boundary tracking for intravital microscopy via multiscale gradient vector flow snakes, IEEE Transactions on Biomedical Engineering 51 (2004) 316–324.

[32] J. Tang, A multi-direction GVF snake for the segmentation of skin cancer images, Pattern Recognition 42 (6) (2009) 1172–1179.

[33] N. Ray, S. Acton, Motion gradient vector flow: an external force for tracking rolling leukocytes with shape and size constrained active contours, IEEE Transactions on Medical Imaging 23 (12) (2004) 1466–1478.

[34] O. Michailovich, Y. Rathi, A. Tannenbaum, Image segmentation using active contours driven by the Bhattacharyya gradient flow, IEEE Transactions on Image Processing 16 (11) (2007) 2787–2801.

[35] M. Keuper, H. Burkhardt, O. Ronneberger, J. Padeken, P. Heun, Mean shift gradient vector flow: A robust external force field for 3d active surfaces, in: 20th International Conference on Pattern Recognition, 2010, pp. 2784–2787.

[36] H. Zhou, G. Schaefer, A. Sadka, M. Celebi, Anisotropic mean shift based fuzy c-means segmentation of dermoscopy images, IEEE Journal of Selected Topics in Signal Processing 3 (1) (2009) 26–34.

[37] H. Zhou, G. Schaefer, M. Celebi, M. Fei, Bayesian image segmentation with mean shift, in: International Conference on Image Processing, 2009, pp. 2405–2408.

[38] H. Zhou, G. Schaefer, T. Liu, F. Lin, Segmentation of optic disc in retinal images using an improved gradient vector flow algorithm, Multimedia Tools Appl. 49 (3) (2010) 447–462.

[39] H. Zhou, G. Schaefer, M. E. Celebi, F. Lin, T. Liu, Gradient vector flow with mean shift for skin lesion segmentation, Comp. Med. Imag. and Graph. 35 (2) (2011) 121–127.

[40] R. Courant, D. Hilbert, Methods of Mathematical Physics, New York: Interscience, 1953.

[41] W. Symes, Partial differential equations of mathematical physics, Lecture Notes, Department of Computational and Applied Mathematics, Rice University, United States (2006).

[42] M. R. Hestenes, Optimization Theory: The Finite-Dimensional Case, Wiley, New York, 1975.

[43] B. Hunt, The application of constrained least squares estimation to image restoration by digital computer, IEEE Transactions on Computers 22 (9) (1973) 805–612.

[44] M.-K. Hu, Visual pattern recognition by moment invariants, Information Theory, IEEE Transactions on 8 (2) (1962) 179–187.

[45] J. Flusser, T. Suk, S. Saic, Recognition of blurred images by the method of moments, IEEE Transactions on Image Processing 5 (3) (1996) 533–538.

[46] T. Chan, H.-M. Zhou, Total variation wavelet thresholding, Journal of Scientific Computing 32 (2) (2007) 315–341.

[47] A. Tsai, A. Y. Jr., A. Willsky, Curve evolution implementation of the mumford-shah functional for image segmentation, denoising, interpolation, and magnification, IEEE Transactions on Image Processing 10 (8) (2001) 1169–1186.

[48] K. Fukunaga, L. Hostetler, The estimation of the gradient of a density function, with applications in pattern recognition, IEEE Transactions on Information Theory 21 (1) (1975) 32–40.

[49] Z.-Q. Wen, Z.-X. Cai, Convergence analysis of mean shift algorithm, Journals of Software 18 (2) (2007) 205–212.

[50] C. Xu, J. Prince, Global optimality of gradient vector flow, in: Proc. of 34th Annual Conference on Information Sciences and Systems, 2000.

[51] G. Argenziano, H. Soyer, V. De Giorgi, Dermoscopy: A Tutorial, EDRA Medical Publishing & New Media, 2002.

[52] J. Staal, A. Niemeijer, M. Viergever, B. van Ginneken, Ridge based vessel segmentation in color images of the retina, IEEE Transactions on Medical Imaging 23 (2004) 501–509.